






Article

Crystal Structure and Magnetic Properties of Peacock–Weakley Type Polyoxometalates $\text{Na}_9[\text{Ln}(\text{W}_5\text{O}_{18})_2]$ ($\text{Ln} = \text{Tm}, \text{Yb}$): Rare Example of Tm(III) SMM

Oleksandra Yu. Mariichak ¹, Sandra Kaabel ^{2,†}, Yevgen A. Karpichev ²,
Georgiy M. Rozantsev ¹, Serhii V. Radio ^{1,*}, Céline Pichon ³, H el ene Bolvin ⁴ and
Jean-Pascal Sutter ^{3,*}

¹ Department of Inorganic, Organic and Analytical Chemistry, Faculty of Chemistry, Biology and Biotechnology, Vasyly' Stus Donetsk National University, 21021 Vinnytsia, Ukraine; o.mariichak@donnu.edu.ua (O.Y.M.); g.rozantsev@donnu.edu.ua (G.M.R.)

² Department of Chemistry and Biotechnology, Division of Chemistry, School of Science, Tallinn University of Technology, 19086 Tallinn, Estonia; sandra.kaabel@taltech.ee (S.K.); yevgen.karpichev@ttu.ee (Y.A.K.)

³ Laboratoire de Chimie de Coordination (LCC-CNRS), Universit e de Toulouse, CNRS, 31077 Toulouse, France; celine.pichon@lcc-toulouse.fr

⁴ Laboratoire de Chimie et de Physique Quantiques, Universit e de Toulouse, CNRS, 31400 Toulouse, France; bolvin@irsamc.ups-tlse.fr

* Correspondence: radio@donnu.edu.ua (S.V.R.); jean-pascal.sutter@lcc-toulouse.fr (J.-P.S.)

† Present address: Department of Chemistry, McGill University, 801 Sherbrooke Street West, Montreal, QC H3A 0B8, Canada.

Received: 1 October 2020; Accepted: 16 October 2020; Published: 21 October 2020



Abstract: We report Peacock–Weakley complexes, $\text{Na}_9[\text{Ln}(\text{W}_5\text{O}_{18})_2]\cdot 35\text{H}_2\text{O}$, formed with Tm(III), **1**, and Yb(III), **2**. Their syntheses, physico-chemical characterizations, crystal structures, and magnetic properties are described. Ab initio calculations are also reported. These polyoxometalate (POM) complexes were obtained using original synthetic conditions where acidification was performed with a stoichiometric amount of nitric acid to an acidity of $Z = \nu(\text{H}^+)/\nu(\text{WO}_4^{2-}) = 8/10 = 0.80$. Both the Tm(III) and Yb(III) derivatives were found to exhibit field-induced slow relaxation of their magnetization likely controlled by Raman and Orbach relaxation processes. **1** is a rare example of a Tm(III)-based single-molecule magnet (SMM) and is a consequence of the oblate tetragonal anti-prismatic symmetry of the coordination sphere.

Keywords: thulium; ytterbium; polyoxometalates; single-molecule magnet; Peacock–Weakley

1. Introduction

Single-molecule magnets (SMMs) are paramagnetic molecules exhibiting a slow relaxation of the magnetization and magnetic hysteresis akin to bulk magnets [1]. The first observation of magnet-like behavior in mononuclear lanthanide complexes in 2003 [2] stimulated tremendous interest. This unique magnetic behavior results from the strong spin-orbit coupling (SOC) and large magnetic moment of Ln(III) ions when the appropriate electronic configuration and geometry are selected. Indeed, first-order SOC leads to quite large and unquenched orbital contributions to the magnetic moment (except for $^1\text{S}_0$ and $^8\text{S}_{7/2}$ ground electronic terms) while the ligand field acts as a weaker perturbation. The lanthanide symmetry and coordination sphere control the local magnetic anisotropy and the relaxation properties as evidenced by numerous magneto-structural studies [3–6].

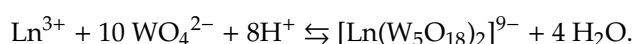
The performances of mononuclear Ln(III) SMMs are enhanced in compounds with highly axial symmetry by the suppression of quantum tunneling of magnetization (QTM), a situation that applies in sandwich-type complexes. The best lanthanide single-center SMM to date is an organometallic Dy(III) complex, $[(\text{Cp}^{iPr5})\text{Dy}(\text{Cp}^*)]^+$ (where Cp^{iPr5} = penta-iso-propylcyclopentadienyl and Cp^* = pentamethylcyclopentadienyl) with a record energy barrier of $U_{\text{eff}}/k_B = 2217$ K resulting in a blocking of the magnetization below 80 K [7]. Polyoxometalates have also been considered as ligands for controlling the coordination geometry of Ln ions. For instance, Peacock–Weakley structures have been shown to impose highly symmetric square antiprism geometry to lanthanides as illustrated with Nd, Tb, Dy, Ho, and Er ions, some of which were found to behave as SMMs [8–10]. Herein, the Tm(III) and Yb(III) homologues were also shown to exhibit slow relaxation of their magnetization.

The syntheses, physico-chemical characterizations, crystal structures, and magnetic properties of Peacock–Weakley complexes, $\text{Na}_9[\text{Ln}(\text{W}_5\text{O}_{18})_2] \cdot 35\text{H}_2\text{O}$, formed with Tm(III), **1**, and Yb(III), **2**, are described. In-field slow relaxation of the magnetization was observed for both derivatives, which is discussed considering the results of *ab initio* calculations. While examples of Yb-based SMMs are well documented [11], only very few Tm derivatives were found to exhibit SMM behaviors, and all appear to be organometallic compounds [12–14].

2. Results and Discussion

2.1. Synthesis

The classical procedure to obtain lanthanide heteropoly anion salts $[\text{Ln}(\text{W}_5\text{O}_{18})_2]^{9-}$ is the protocol proposed by Peacock and Weakley in 1971 [15] in which acetic acid was used for acidification of the solution to pH 7.0–7.5. In the present work, acidification was instead conducted with a stoichiometric amount of nitric acid to an acidity of $Z = \nu(\text{H}^+)/\nu(\text{WO}_4^{2-}) = 8/10 = 0.80$. Acidity $Z = 0.80$ in the presence of stoichiometric amounts of initial ions corresponded to the formation of heteropoly decatungstolanthanidate(III) anions [16–18]:



The equilibria in the systems $[\text{Ln}(\text{W}_5\text{O}_{18})_2]^{9-} - \text{H}^+(\text{OH}^-) - \text{H}_2\text{O}$ (Ln = Nd, Gd, Ho) at various Z ranges were previously studied by pH–potentiometry and mathematical modeling [16–18]. This showed that, at $Z = 0.80$, the ions $[\text{Ln}(\text{W}_5\text{O}_{18})_2]^{9-}$ (50 mol.%) and $\text{H}[\text{Ln}(\text{W}_5\text{O}_{18})_2]^{8-}$ (35 mol.%), are predominant in the solution with molar amounts of the WO_4^{2-} and $[\text{Ln}(\text{W}_5\text{O}_{18})(\text{H}_2\text{O})_n]^{3-}$ ions. A typical synthesis of Peacock–Weakley complexes in acetic acid acidified solution leads to the formation of a buffer solution, which facilitates both the formation of acid salts as well as the possible hydrolysis of high-charge anions.

This leads to the isolation of either neutral or acid salts. For example at pH 7.0–7.5, $\text{H}_n[\text{Ln}(\text{W}_5\text{O}_{18})_2]^{(9-n)-}$ ($n = 1-3$) species are predominant, whereas the acid salts are stabilized at lower pH values and $[\text{Ln}(\text{W}_5\text{O}_{18})_2]^{9-}$ salts favored at higher pH values. Thus, salts with different numbers of hydrogen atoms (0–3) were obtained at very close pH values: $\text{Na}_9[\text{Ln}(\text{W}_5\text{O}_{18})_2] \cdot 35\text{H}_2\text{O}$ (Ln = Tb, Dy; pH 7.4–7.5) [19,20], $\text{Na}_9[\text{Ln}(\text{W}_5\text{O}_{18})_2] \cdot 35\text{H}_2\text{O}$ (Ln = Nd, Tb, Dy, Ho, Er; pH 7.2) [8,9], $\text{Na}_9[\text{Eu}(\text{W}_5\text{O}_{18})_2] \cdot n\text{H}_2\text{O}$ ($n = 32$ [21], $n = 35$ [22]; pH 7.0–7.5), $\text{Na}_8\text{H}[\text{Gd}(\text{W}_5\text{O}_{18})_2] \cdot 30\text{H}_2\text{O}$ (pH 7.3) [23], $\text{K}_3\text{Na}_4\text{H}_2[\text{Gd}(\text{W}_5\text{O}_{18})_2] \cdot 21\text{H}_2\text{O}$ (pH 7.3) [24], $\text{Na}_7\text{H}_2[\text{Ln}(\text{W}_5\text{O}_{18})_2] \cdot n\text{H}_2\text{O}$ (Ln = La, Ce, Pr, Nd, Sm, Eu, Gd, Dy, Ho, Er, Yb; pH 7.2) [25], and $\text{Na}_6\text{H}_3[\text{Sm}(\text{W}_5\text{O}_{18})_2] \cdot 28\text{H}_2\text{O}$ (pH 7.0) [26].

Such a situation does not apply with nitric acid. HNO_3 does not lead to the formation of a buffer solution and allows us to consider the H^+ ions introduced as a reactant that is completely consumed in the self-assembly reaction of the anion $[\text{Ln}(\text{W}_5\text{O}_{18})_2]^{9-}$. Following this approach, the heteropoly anions $[\text{Ln}(\text{W}_5\text{O}_{18})_2]^{9-}$ with Ln = Tm (**1**) or Yb (**2**) were crystallized by slow evaporation.

Solid state infrared spectra of the two complexes have been collected showing the characteristic O–W–O bands of the POM (See Experimental section). Scanning electron microscopy (SEM) suggested single-phases for the synthesized salts **1** and **2** as SEM-images of triturated samples showed no zones

with different surface morphology (Supporting Information, Figures S12–S15). This was confirmed by X-ray powder diffraction data (Figure S3).

2.2. Crystal Structures

The structures for **1** and **2** were solved using single crystal X-ray diffraction. The main crystallographic data and refinement parameters are given in Table 1. Compounds **1** and **2** crystallize in the triclinic *P*-1 space group and their crystal structures are shown in Figure 1, Figures S1 and S2. The lanthanide atoms are sandwiched between two $[W_5O_{18}]^{6-}$ units, which behave as tetradentate ligands and may be regarded as derived by the removal of one terminal WO_4^{4+} group from the Lindqvist anion $[W_6O_{19}]^{2-}$ (Figure 1).

Table 1. Selected crystallographic data and refinement parameters of **1** and **2**.

	1	2
Formula ^a	Na ₉ TmW ₁₀ O ₇₁ ^a	Na ₉ YbW ₁₀ O ₇₁ ^a
Mw (g mol ⁻¹)	3350.34	3354.45
Crystal system	triclinic	triclinic
Space group	<i>P</i> -1	<i>P</i> -1
<i>T</i> (K)	100(2)	100(2)
<i>a</i> (Å)	12.7285(2)	12.7285(2)
<i>b</i> (Å)	13.0501(3)	13.0447(3)
<i>c</i> (Å)	20.4565(6)	20.4508(5)
α (°)	82.870(2)	82.836(2)
β (°)	74.392(3)	74.478(2)
γ (°)	88.718(3)	88.747(2)
<i>V</i> (Å ³)	3247.2(2)	3246.0(1)
<i>Z</i>	2	2
ρ calcd. (g cm ⁻³)	3.427	3.432
μ (mm ⁻¹)	1.54184	1.54184
Collected reflns	11,324	11,373
Unique reflns	10,563	11,096
<i>R</i> _{int}	0.0627	0.0318
Final <i>R</i> ₁ , <i>wR</i> ₂ (<i>I</i> ≥ 2σ) ^{b,c}	0.0533, 0.1510	0.0261, 0.0677
<i>R</i> ₁ , <i>wR</i> ₂ (all data)	0.0567, 0.1555	0.0277, 0.0689
GOF on <i>F</i> ² ^d	1.097	1.107
ICSD ref.	1,960,251	1,960,252

^a Excluding the hydrogen atoms on the water molecules that were not located, ^b $R_1 = \sum ||F_o| - |F_c|| / \sum |F_o|$,
^c $wR_2 = [\sum (w(F_o^2 - F_c^2)^2) / \sum (w(F_o^2)^2)]^{1/2}$ where $w = 1/(\sigma^2(F_o^2) + (aP)^2 + bP)$ with $P = (2F_c^2 + \max(F_o^2, 0)) / 3$.
^d $GOF = [\sum w(F_o^2 - F_c^2)^2 / (n - p)]^{1/2}$, where *n* is the number of reflections and *p* is the number of parameters.

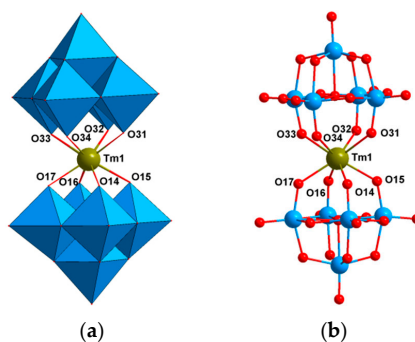


Figure 1. The molecular structure for $[Tm(W_5O_{18})_2]^{9-}$, **1**: (a) Polyhedra and (b) ball and stick views. Color scheme: WO_6 = blue polyhedral, W = blue, Tm = bronze and O = red.

The central Ln(III) cation is coordinated by eight terminal oxygen atoms adopting a square antiprism geometry with a D_{4d} pseudosymmetry. The evaluation of the polyhedral shapes by continuous shape measures [27,28] performed with SHAPE [29] indicated that the geometry around the lanthanide is highly symmetric and extremely close to an ideal square antiprism (Figure 1 and Table S1; shape value of 0.066 (**1**) and 0.063 (**2**) compared to 0 for an ideal geometry). The Ln–O bond lengths (Table 2) are in the range 2.31–2.38 Å (mean value 2.35 Å) for **1**, and 2.33–2.36 Å (mean value 2.34 Å) for **2**; the related bond angles are gathered in Table 3. The heteropoly anions are surrounded by a network of H₂O-coordinated Na⁺ cations balancing their anionic charge and introducing 35 H₂O molecules in the lattice, as was previously observed for other sodium salts with decatungstolanthanide anions [8–10,19,20]. This complex system of hydrogen bonds and the bulkiness of the POM ligands resulted in an excellent isolation of the Ln(III) ions in the solid state with shortest lanthanide–lanthanide distances of 11.21 and 12.46 Å for **1** and **2**, respectively (Figures S1c and S2d).

Table 2. Selected bond lengths of **1** and **2** (Å).

Compound 1					
Tm1–O16	2.348(7)	Tm1–O32	2.385(8)	Tm1–O33	2.347(7)
Tm1–O31	2.355(8)	Tm1–O15	2.338(7)	Tm1–O14	2.309(8)
Tm1–O17	2.348(8)	Tm1–O34	2.364(8)		
Compound 2					
Yb1–O34	2.348(4)	Yb1–O31	2.363(4)	Yb1–O17	2.316(4)
Yb1–O14	2.336(4)	Yb1–O33	2.356(4)	Yb1–O32	2.348(4)
Yb1–O15	2.330(4)	Yb1–O16	2.342(4)		

Table 3. Selected bond angles of **1** and **2** (°).

Compound 1			
O16–Tm1–O32	75.9(3)	O16–Tm1–O31	140.8(3)
O16–Tm1–O17	73.8(3)	O16–Tm1–O34	143.0(2)
O33–Tm1–O16	77.3(3)	O33–Tm1–O32	73.7(3)
O33–Tm1–O31	115.1(3)	O33–Tm1–O17	73.8(3)
O33–Tm1–O34	73.3(3)	O31–Tm1–O32	73.0(3)
O31–Tm1–O34	73.6(3)	O15–Tm1–O16	73.8(3)
O15–Tm1–O32	77.5(3)	O15–Tm1–O33	143.2(2)
O15–Tm1–O31	73.6(3)	O15–Tm1–O17	118.0(3)
O15–Tm1–O34	141.4(2)	O14–Tm1–O16	117.5(3)
O14–Tm1–O32	144.1(2)	O14–Tm1–O33	139.7(3)
O14–Tm1–O31	78.3(3)	O14–Tm1–O15	75.2(3)
O14–Tm1–O17	75.2(3)	O14–Tm1–O34	75.1(3)
O17–Tm1–O32	139.4(2)	O17–Tm1–O31	144.4(2)
O17–Tm1–O34	76.9(4)	O34–Tm1–O32	115.5(3)
Compound 2			
O14–Yb1–O34	76.5(1)	O14–Yb1–O31	77.5(1)
O14–Yb1–O33	141.4(1)	O14–Yb1–O32	142.9(1)
O14–Yb1–O16	117.9(1)	O33–Yb1–O31	115.6(1)
O32–Yb1–O34	115.2(1)	O32–Yb1–O31	73.3(1)
O32–Yb1–O33	73.5(1)	O15–Yb1–O34	140.5(1)
O15–Yb1–O31	75.6(1)	O15–Yb1–O14	73.7(1)
O15–Yb1–O33	143.2(1)	O15–Yb1–O32	77.2(1)
O15–Yb1–O16	73.9(1)	O16–Yb1–O34	144.4(1)
O16–Yb1–O31	139.2(1)	O16–Yb1–O33	77.1(1)
O16–Yb1–O32	74.1(1)	O17–Yb1–O34	78.3(1)
O17–Yb1–O31	144.3(1)	O17–Yb1–O14	75.1(1)
O17–Yb1–O33	75.3(1)	O17–Yb1–O32	140.0(1)
O17–Yb1–O15	117.3(1)	O17–Yb1–O16	75.1(1)
O34–Yb1–O31	73.2(14)	O34–Yb1–O33	73.6(1)

2.3. Magnetic Properties

The temperature dependence of the molar magnetic susceptibility, χ_M , for **1** and **2** between 2 and 300 K is depicted as $\chi_M T = f(T)$ in Figure 2. The values of 7.03 (**1**) and 2.50 (**2**) $\text{cm}^3 \text{K mol}^{-1}$ at 300 K are consistent with anticipated contributions for isolated ions (7.15 $\text{cm}^3 \text{K mol}^{-1}$ for Tm(III) with a $^3\text{H}_6$, $S = 1$, $L = 5$, $g_6 = 7/6$ ground state, and 2.57 $\text{cm}^3 \text{K mol}^{-1}$ for Yb(III) with $^2\text{H}_{7/2}$, $S = 1/2$, $L = 3$, $g_{7/2} = 8/7$ ground state). When the temperature decreased, $\chi_M T$ continuously diminished for both compounds with a more rapid decrease below 10 K, reaching 5.8 $\text{cm}^3 \text{K mol}^{-1}$ for **1** and 1.26 $\text{cm}^3 \text{K mol}^{-1}$ for **2** at 2 K. These thermal dependences of $\chi_M T$ are due to the depopulation of the excited electronic (Stark) levels due to the crystal field effect. The field dependence of the magnetization recorded at 2 K (Figure 2) showed a rapid increase for low fields, and, above ca. 15 kOe, a very smooth augmentation to reach of 3.6 μ_B (**1**) and 2.0 μ_B (**2**) at 50 kOe; no hysteresis was observed. These values are similar to those reported for Tm(III) [12,14] and Yb(III) [30,31] systems, and they confirm that there is an important splitting of the ground J manifold by the ligands [32,33]. For the ground state with a pure M_J term, the saturation magnetization is given by $M_S = \frac{1}{2} \times J \times g_J$. The M_S values found for **1** and **2** suggest that the doublets with largest M_J (± 6 for Tm(III) and between $\pm 7/2$ and $\pm 5/2$ for Yb(III)) are the ground states.

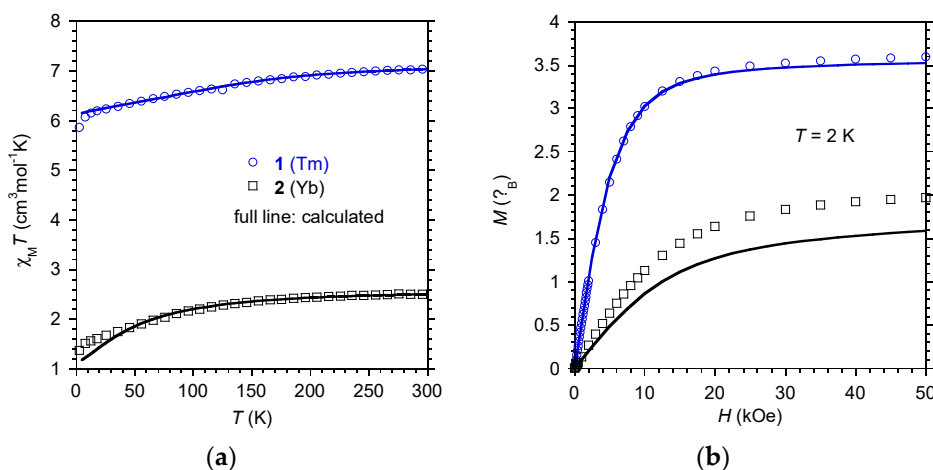


Figure 2. (a) Temperature dependence of $\chi_M T$ and (b) magnetization at 2 K for the complexes **1** (in blue) and **2** (in black). Full lines correspond to the ab initio calculated behaviors.

AC susceptibility studies were performed to probe the presence of slow magnetic relaxation in **1** and **2**. In a zero field, an onset of the out-of-phase susceptibility (χ_M'') component was found for the complexes, while, with the applied DC field, this emerged for all AC frequencies (Figures S4 and S8). Fast quantum tunneling of the magnetization (QTM) was likely operating at zero field and was reduced/suppressed with the field that lifted the energy level degeneracy of the m_J states. For **1**, the longest relaxation time was found for $H_{\text{DC}} = 3 \text{ kOe}$, which was selected as the optimal field. For **2**, while the maximum of the $\chi_M'' = f(\nu)$ curves shifted to lower frequencies with the field, a decrease of intensity was observed for $H_{\text{DC}} > 1.2 \text{ kOe}$ (Figure S8); therefore, 1.2 kOe was chosen as the optimal field for **2**. These respective fields were applied for the subsequent AC studies.

2.3.1. AC Behavior for $\text{Na}_9[\text{Tm}(\text{W}_5\text{O}_{18})_2]$, **1**:

The frequency dependence of the AC signals for **1** was collected between 2 and 30 K for the frequency range 1–1500 Hz in a field of 3 kOe (Figure 3 and Figure S5). The data were fitted at each temperature using a generalized Debye model affording the relaxation time τ [34]. The thermal dependence of τ (Figure 3) clearly indicated the contribution of at least two relaxation mechanisms. This is supported by the distribution width, α , of the relaxation times deduced at each temperature by

the analysis of the Cole–Cole plots ($\chi_M'' = f(\chi_M')$, Figure S6) [35]. The values ranged between 0.01 for the high T domain to 0.28 at low T suggesting several contributions to the relaxation at lower temperatures. Spin-phonon processes, such as Raman, Orbach, and field-induced direct pathways, as well as QTM, may concomitantly be operating in the relaxation of mononuclear complexes [36,37]. In the expression of τ^{-1} , given in equation 1, the terms from left to right account, respectively, for the direct, QTM, Raman, and Orbach process, where A , B , C , and n are coefficients and H is the magnetic field, T is the temperature, U_{eff} is the energy barrier, and τ is the pre-exponential time.

$$\tau^{-1} = AH^2T + \frac{B}{1 + B_2H^2} + CT^n + \tau_0^{-1} \exp\left(\frac{-U_{\text{eff}}}{k_B T}\right) \quad (1)$$

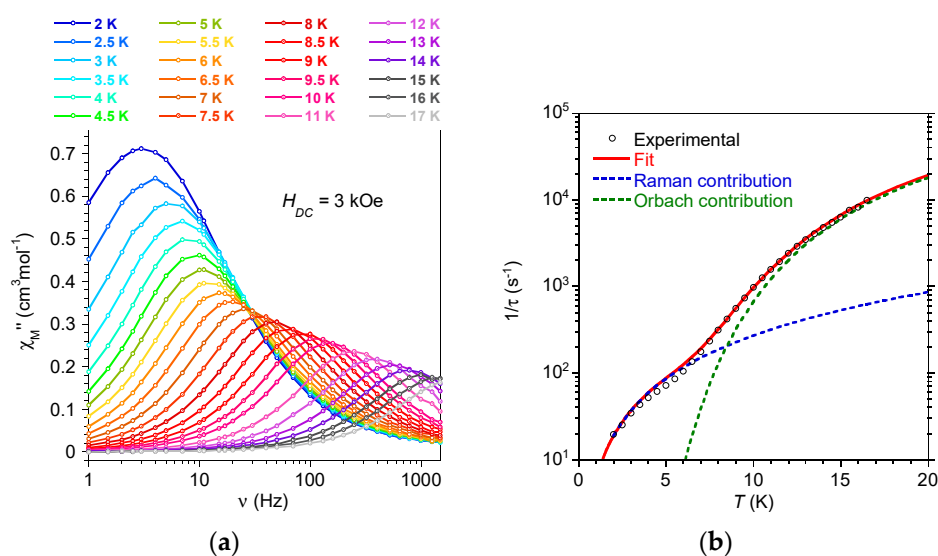


Figure 3. (a) Frequency dependence of the out-of-phase component of the AC susceptibility of **1** with an applied field of 3 kOe, and (b) temperature dependence of its relaxation time with the best fit (—) for a combination of Raman, and Orbach contributions, and (---) their calculated individual contributions.

Since the AC signal was collected in field, the QTM is expected to be cancelled; conversely, a degree of relaxation by a direct pathway might be expected. Therefore, direct, Raman, and Orbach pathways were considered to model the relaxation behavior of **1**. The variation of τ over the whole temperature range was best reproduced for a combination of Raman and Orbach contributions (Figure 3b) with the following set of parameters: $C = 6 \pm 16 \text{ s}^{-1} \text{K}^{-n}$, $n = 2 \pm 1$, $\tau_0 = 2.1 \pm 0.3 \times 10^{-6} \text{ s}$, and $U_{\text{eff}}/k_B = 66 \pm 3 \text{ K}$. However, the obtained U_{eff} is far smaller than the energy gap between the ground and first excited level by theoretical calculations (vide infra). Fairly good modeling was also obtained when the Raman and direct processes were considered (Figure S7a). Tentative modeling with other combinations of relaxation pathways gave poor results (see Figure S7). It appears, therefore, likely that the relaxation for **1** is mainly driven by a Raman pathway.

To date, the only reported POM-based Tm(III) complex is $[\text{TmP}_5\text{W}_{30}\text{O}_{110}]^{12-}$ polyoxometalate but no SMM properties were found in this case [38]. Four organometallic Tm(III) compound incorporating the COT ligand were also reported to exhibit slow relaxation of the magnetization governed by several relaxation pathways. For $[(\text{Tp}^*)\text{Tm}_{0.05}\text{Y}_{0.95}(\text{COT})]$, the analysis of the relaxation behavior by the Raman and Orbach processes gave an energy barrier of 111 K while for the homologous $[(\text{Tp})\text{Tm}_{0.05}\text{Y}_{0.95}(\text{COT})]$, an energy barrier of 46 K was reported [12]. $[\text{K}(\text{18-crown-6})(\text{THF})_2][\text{Tm}(\text{COT})_2]$ was reported with an energy barrier $U_{\text{eff}}/k_B = 53.3 \text{ K}$ whereas $[\text{Tm}(\text{COT})(\text{THF})_2]$, showed SMM behaviors exclusively under applied fields with a small energy barrier around 8 K [14]. $[\text{Tm}^{\text{III}}(\text{DMF})_4(\text{H}_2\text{O})_3\text{Co}^{\text{III}}(\text{CN})_6]$ is another example of a Tm(III) complex with field-induced slow relaxation of the magnetization induced

by the QTM, Raman, and Orbach pathways ($U_{\text{eff}}/k_B = 25$ K) [13]. Thus, compound **1** belongs to a very short-list of Tm(III)-based SMMs (Table 4).

Table 4. Tm^{III}-based SMMs reported in the literature and their characteristics.

Compound	H_{dc} (Oe)	τ_0 (s)	U_{eff} (K)	C (s ⁻¹)	n	τ_{QTM} (s)	Ref.
[Tp(Tm)(COT)]	2000	$4.7(9) \times 10^{-7}$	111(2) 130(1)		4.21(3)		Meng [12]
[Tp*(Tm)(COT)]	2000	$2.4(2) \times 10^{-6}$	46(1)	n.c.	3.91(6)		Meng [12]
[Tm(COT)](THF) ₂	800	1.18×10^{-4}	7.93	0.059	6.2	2.68×10^{-3}	Harriman [14]
[K(18-C-6)(THF) ₂][Tm(COT) ₂]	200	1.28×10^{-4}	53.3	0.010	3.66	0.371	Harriman [14]
[Tm(dmfa) ₄ (H ₂ O) ₃ Co(CN) ₆]	1000	$3.2(2) \times 10^{-7}$	22(1)	6.8(1)	5.4(2)		Amjad [13]
Na ₉ [Tm(W ₅ O ₁₈) ₂] (1)	3000	$2.1(1) \times 10^{-6}$	66(3)	6(16)	2(1)		this work

2.3.2. AC Behavior for Na₉[Yb(W₅O₁₈)₂], **2**

The AC susceptibility behavior recorded for Yb-derivative **2** between 2 and 10 K with $H_{\text{DC}} = 1.2$ kOe is depicted in Figure 4 and Figure S9. Analysis of the Cole–Cole plots (Figure S10) revealed a distribution width of the relaxation times ranging from $\alpha = 0.09$ at 6.5 K to 0.23 at 2 K. The larger α value at lower temperatures again suggest that different processes contribute to the relaxation of the magnetization. As for **1**, the best modeling of the variation of τ with temperature was obtained for a relaxation driven by Raman and Orbach pathways with best-fit parameters $C = 85 \pm 42$ s⁻¹ K⁻ⁿ, $n = 1.8 \pm 0.4$, $\tau_0 = 7.1 \pm 1 \times 10^{-8}$ s and $U_{\text{eff}}/k_B = 47 \pm 5$ K (33 ± 3 cm⁻¹). The obtained effective energy barrier U_{eff} is about half the energy gap between ground and first excited Kramers doublet by theoretical calculations (vide infra). Tentative modeling with other combinations of relaxation pathways can be found in Figure S11.

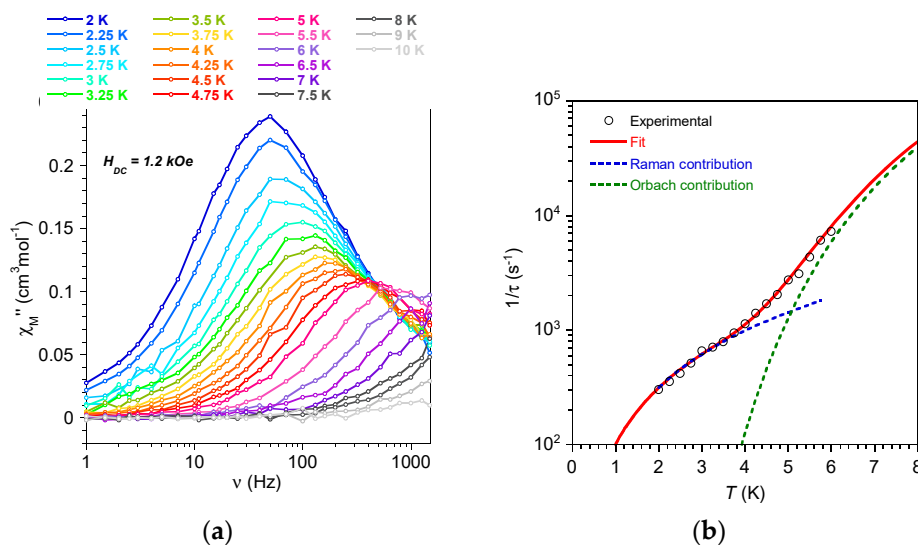


Figure 4. (a) The frequency dependence of the out-of-phase component of the AC susceptibility of **2** with an applied field of 1.2 kOe, and (b) temperature dependence of its relaxation time with the best fit (—) for a combination of Raman and Orbach contributions, and (---) their calculated individual contributions.

Slow relaxation of the magnetization is common for Yb(III) complexes [11]; however, only one POM-based Yb(III) compound, $[\text{Yb}(\beta_2\text{-SiW}_{11}\text{O}_{39})_2]^{13-}$, was reported to show such a behavior [9], but its SMM characteristics were not established due to temperature limitations. Complex **2** appears to be the first example of a POM-based Yb derivative with well-defined in-field SMM behavior.

2.4. Ab Initio Calculations

The energies of **1** and **2** were determined using the ab initio SO-CASSCF method, as given in Table S2. The ground terms of the free ions, $^3\text{H}_6$ for Tm(III) and $^2\text{H}_{7/2}$ for Yb(III), are split by about

400 cm^{-1} by the ligands. The symmetry of the coordination sphere in $[\text{Ln}(\text{W}_5\text{O}_{18})_2]^{9-}$ complexes is remarkably close from D_{4d} , and, in this symmetry, M_J is a good quantum number for an axial symmetry. In the following, the pseudo C_4 axis will be denoted as the z and quantification axis. The states of complex **2** are Kramers doublets (KDs), with an almost pure composition in terms of M_J , the $\pm 5/2$ being the ground doublet. The $\pm 7/2$ doublet lies 65 cm^{-1} above. The $\chi_M T$ deduced from this SO-CASSCF calculations fits well the experimental curve, but the magnetization at 2 K is too small. We checked whether a ground $M_J = \pm 7/2$ KD would better fit the experimental data: this would provide a plateau slightly too high for the magnetization, and the $\chi_M T$ values at low temperature would be much higher. This confirms that the $\pm 5/2$ doublet is the ground one. g factors are given in Table S3. They are as expected for pure M_J doublets: all KDs denote an axial magnetic moment, except the $\pm 1/2$ one, and the 2nd KD is more magnetic than the ground one.

For complex **1**, the states form non-Kramers doublets (NKDs) with small energy gaps, except state number 7. The ground NKD is almost a pure $M_J = \pm 6$ doublet, but the other states denote strong mixings between different M_J values. This might be due to their energetic vicinity. The ground NKD is well separated from the excited states by an energy of more than 300 cm^{-1} , while all the other states issued from the ground J are grouped together. The g factors deduced from the NKDs are given in Table S3. We remind here that only one principal value of the g tensor is worth non-zero for an NKD.

The direction of the magnetic moment of the ground NKD is along the z axis, while it takes an oblique direction for other doublets, for finally lying in the equatorial plane for the last doublet. The magnetic properties of the ground NKDs are favorable to slow relaxation of its magnetic moment: the energy gap of the NKD is very tiny, 0.012 cm^{-1} , which quenches the tunneling between the two directions and the doublet is well separated from the other states with an energy gap of 330 cm^{-1} with the first excited state. Such a large barrier could not be evidenced in the analysis of the temperature dependence of τ . This strongly suggests that the relaxation of the magnetization in **1** is not driven by an Orbach pathway but by a faster process, such as a vibronic (Raman) process.

The crystal field parameters (CFPs) were deduced from the ground J manifold using the ITO technique and are given in Table S4. They are similar in the two complexes, with a small decrease along the series, as is usually the case [39]. The strength parameters are of the same order of magnitude as other late-lanthanide complexes with O-donor ligands. This is dominated by 2nd and 4th orders, and only the parameters of index 0, B_0^k ($k = 2, 4, 6$), are important, due to the quasi D_{4d} symmetry. Consequently, S_0 S_0 is by far dominant, and S_4 would be important in a D_{4h} . B_0^2 is negative as expected from an axially compressed O_8 coordination core leading to an oblate environment (Figure S1d). This type of coordination sphere stabilizes the states with a prolate electron density, and these states have large values of $|M_J|$ for the late lanthanides [40]. In **1** and **2**, the oblate O_8 core results in ground states with the largest $|M_J|$ for Tm(III) and the second largest for Yb(III), and the pseudo D_{4d} symmetry leads to doublets that are pure in terms of M_J . The magnetic moments are consequently large and axial, along the C_4 axis.

3. Materials and Methods

3.1. Syntheses

All reagents and solvents were used as received from commercial sources. Nitric acid solution ($C = 0.4832 \text{ mol L}^{-1}$) was prepared from concentrated HNO_3 (chemically pure grade). The exact concentration was determined by titration of a weighed amount of sodium tetraborate (methyl red indicator) ($\delta = 0.5\%$) [41]. Recrystallized sodium tetraborate decahydrate $\text{Na}_2\text{B}_4\text{O}_7 \cdot 10\text{H}_2\text{O}$ was used for standardization; the H_2O content was determined gravimetrically based on the weight loss after isothermal calcination (773 K) [41]. $\text{Tm}(\text{NO}_3)_3$ ($C = 0.2933 \text{ mol L}^{-1}$) and $\text{Yb}(\text{NO}_3)_3$ ($0.2351 \text{ mol L}^{-1}$) solutions were prepared by dissolving Tm_2O_3 and Y_2O_3 in HNO_3 . Excess amounts of HNO_3 were removed by two-fold evaporation until wet residues were formed, which were then dissolved in distilled water. The concentrations of Tm(III) and Yb(III) were determined by direct complexometric

titration using Trilon B solution (analytically pure grade) in acetate buffer solution with pH 5.5 (xylenol orange indicator) ($\delta = 0.8\%$) [42].

$\text{Na}_9[\text{Tm}(\text{W}_5\text{O}_{18})_2]\cdot 35\text{H}_2\text{O}$, **1**: $\text{Na}_2\text{WO}_4\cdot 2\text{H}_2\text{O}$ (3.2980 g, 10.00 mmol) was dissolved in distilled water (80.03 mL). Then, HNO_3 solution (16.56 mL, $C = 0.4832\text{ mol L}^{-1}$, 8 mmol) was added dropwise with vigorous stirring. A solution of $\text{Tm}(\text{NO}_3)_3$ (3.41 mL, $C = 0.2933\text{ mol L}^{-1}$, 1 mmol) was added dropwise and very slowly to the acidified tungstate solution with vigorous stirring. The final volume of the solution was 100 mL. The solution was stored for 2 weeks at room temperature leading to the formation of a needle-like crystalline precipitate of **1**. The solid was filtered, washed with cold water, and air dried. The yield was 48%. IR (KBr, cm^{-1}): 3449 (br, $\nu(\text{O-H})$), 1637 (s, $\delta(\text{H}_2\text{O})$), 933 (s, $\nu(\text{W=O})$), 849 (s, $\nu(\text{O-W-O})$), 791 (m), 715(s), 582 (w), 544 (w), 492 (w), 480 (w), 422 (w, $\delta(\text{O-W-O})$). Raman (cm^{-1}): 947 (s), 889 (s), 838 (m), 712 (w), 544 (w), 427 (w), 343 (m), 175 (s). Elemental analysis (%) calcd. for $\text{Na}_9[\text{Tm}(\text{W}_5\text{O}_{18})_2]\cdot 35\text{H}_2\text{O}$: Na 6.05, Tm 4.94, W 53.74, H 2.06; found: Na 6.1, Tm 4.8, W 53.5, H 2.0.

$\text{Na}_9[\text{Yb}(\text{W}_5\text{O}_{18})_2]\cdot 35\text{H}_2\text{O}$, **2**: $\text{Na}_2\text{WO}_4\cdot 2\text{H}_2\text{O}$ (3.2980 g, 10.00 mmol) was dissolved in distilled water (80.03 mL). Then, a HNO_3 solution (16.56 mL, $C = 0.4832\text{ mol L}^{-1}$, 8 mmol) was added dropwise with vigorous stirring. A solution of $\text{Yb}(\text{NO}_3)_3$ (4.25 mL, $C = 0.2351\text{ mol L}^{-1}$, 1 mmol) was added dropwise and very slowly to the acidified tungstate solution with vigorous stirring. The final volume of the solution was 79.19 mL. The solution was stored for 2 weeks at room temperature leading to the formation of a needle-like crystalline precipitate of **1**. The solid was filtered, washed with cold water, and air dried. Yield 52%. IR (KBr, cm^{-1}): 3444 (br, $\nu(\text{O-H})$), 1636 (s, $\delta(\text{H}_2\text{O})$), 934 (s, $\nu(\text{W=O})$), 848 (s, $\nu(\text{O-W-O})$), 792 (m), 710(s), 585 (w), 547 (w), 490 (w), 421 (w, $\delta(\text{O-W-O})$). Raman, cm^{-1} : 948 (s), 889 (s), 830 (m), 720 (w), 544 (w), 427 (w), 343 (m), 200 (s). Elemental analysis (%) calcd. for $\text{Na}_9[\text{Yb}(\text{W}_5\text{O}_{18})_2]\cdot 35\text{H}_2\text{O}$: Na 6.04, Yb 5.05, W 53.68, H 2.06; found: Na 6.2, Tm 5.0, W 53.6, H 2.1.

3.2. Fourier Transform Infrared (FT-IR)

FT-IR spectroscopy was performed on air-dried samples in a KBr matrix (content of the sample in KBr matrix was 0.5 wt%) using the Perkin-Elmer FTIR Spectrum BXII infrared spectrometer (Waltham, MA, USA) from 400 to 4000 cm^{-1} . The Raman spectra were obtained at room temperature using CARS confocal laser scanning microscopes (SOL Instruments, Minsk, Belarus). The spectra were excited using a He-Ne laser (632.8 nm). The radiation power on the sample was 4.7 mWt. The time of signal accumulation was one second. The Raman spectra were recorded from 100 to 3100 cm^{-1} . All measurements were conducted with a Perkin-Elmer spectrum GX 2000 FT-IR spectrometer three times and averaged.

3.3. Single-Crystal X-ray Diffraction

Single crystals suitable for X-ray diffraction were coated with Fomblin[®] Y oil and mounted onto the goniometer. Single crystal X-ray diffraction data was collected at 100 K on a Rigaku Compact HomeLab diffractometer equipped with a Saturn 944 HG CCD camera, and using monochromatic $\text{Cu-K}\alpha$ -radiation ($\lambda = 1.54184\text{ \AA}$) from a MicroMaxTM-003 sealed tube microfocus X-ray source. The data were collected using ω -scans. CrysAlisPro [43] was used for the data collection and processing, and numerical absorption correction [44] was performed based on a multifaceted crystal model. The structures were solved using SHELXT program and refined by the full-matrix least-squares method against F^2 with SHELXL-2016 through OLEX2 program package [45–47]. The positions of hydrogen atoms were not determined. All non-hydrogen atoms were refined with anisotropic atomic displacement parameters.

3.4. Scanning Electron Microscopy

The investigations of the surface morphology of triturated samples of **1** and **2** by scanning (raster) electron microscopy and X-ray microanalysis were conducted using a complex analytical scanning electron microscope JSM 6490 LV (JEOL) and energy dispersive X-ray (EDX) spectrometer INCA PentaFETx3 (OXFORD Instruments). Imaging of the samples deposited on a conductive graphite tape were carried out in two modes: backscattered electron imaging (BEI) mode for the elemental analysis

of phases constituting the samples and secondary electron imaging (SEI) mode for the study of surface micromorphology of obtained salts. The cathode material was lanthanum hexaboride (LaB_6). The used accelerating voltage was between 10 and 20 kV.

The obtained salts had the composition of **1** and **2**, which was confirmed by the results of EDX performed in different parts of the samples (Figure S12). X-ray spectral microanalysis was carried out for various points of the powder surface. The size of the excitation area at points was up to 5 μm in diameter and up to 5 μm in depth. The obtained atomic fractions of the elements indicated the preservation of the molar ratio $\text{Na:Ln:W} = 9:1:10$ ($\text{Ln} = \text{Tm}$ (**1**), Yb (**2**)) at each point of the studied samples, which agrees with the data of the chemical analysis.

The determination of the chemical composition, surface scanning, and imaging in backscattered electrons (BEC) were performed at an accelerating voltage of 20 kV. Imaging with secondary electrons was carried out at an accelerating voltage of 10 kV. During the scanning, uneven sample surfaces caused an insignificant masking effect on the recorded signal. The uniform contrast of the sample surface, which was recorded in the backscattered electron mode, also indicates its single-phase nature. This was also confirmed by the survey of the samples surface area in the characteristic X-ray emission. Figures S8 and S9 show the uniform distribution of elements (O, Na, Tm, and W for **1**; O, Na, Yb, and W for **2**) over the sample surface without any segregations.

Microscopic analysis showed that the surfaces of the grains of **1** and **2** salts after grinding in an agate mortar had fuzzy blurred edges; the surface of the salt was made of spherical grains whose size was within the range of 100–500 nm for **1** and 200–300 nm for **2** (Figure S10).

3.5. Magnetic Properties

Magnetic studies were carried out with a Quantum Design MPMS-5S SQUID magnetometer (San Diego, CA, USA) with freshly isolated polycrystalline powders mixed with grease and put in gelatin capsules. The data were collected between 300 and 2 K with an applied field of 1 kOe (**1**) and 10 kOe (**2**) and corrected for the diamagnetic contribution sample by using Pascal's tables [32] and for the sample holder. The field dependences of the magnetization were measured at 2 K with the DC magnetic field up to 5 T. The absence of ferromagnetic impurities was checked by the measurement of M vs. H at 100 K. AC susceptibility data were collected in the frequency range 1–1500 Hz with $H_{\text{AC}} = 3$ Oe in zero and with an applied static field.

3.6. Computational Details

The calculations were performed on the $[\text{Ln}(\text{W}_5\text{O}_{18})_2]^{9-}$ complexes ($\text{Ln} = \text{Tm}, \text{Yb}$) based on the X-ray structures using the MOLCAS-7.8 suite of software (www.molcas.org). Relativistically contracted ANO-RCC basis sets of TZP quality were used for Tm, Yb, and O atoms [48,49]. W atoms were described using relativistic AIMP (ab initio model potentials) with the corresponding basis sets 3s3p4d2f for the 12 valence electrons [50]. First, a SF-CASSCF (spin-free CASSCF) calculation was performed [51] with an active space composed of the seven 4f orbitals of the lanthanide ion and associated electrons, that is, CAS(n,7). Spin-orbit (SO) coupling was included by a state interaction with the RASSI (restricted active space state interaction) method [52]. We considered 21 triplets and 28 singlets for Tm and 7 doublets for Yb for the state interaction. Scalar relativistic effects were considered by means of the Douglas-Kroll-Hess transformation [53], and the SO integrals were calculated using the AMFI (atomic mean-field integrals) approximation [54]. The g -values were calculated according to reference [55], and the CFPs were calculated with a local program written in Mathematica as described in [39,56].

4. Conclusions

Two Peacock-Weakley lanthanide complexes ($\text{Ln} = \text{Tm}$ for **1** and Yb for **2**) were synthesized using an original procedure involving HNO_3 in a stoichiometric ratio. This permitted us to circumvent the high sensitivity to pH of the reaction outcome.

In these complexes, the Ln(III) ion sits in a quasi-perfect square antiprism polyhedron and is efficiently isolated from a point view of the magnetic interactions. The two $(W_5O_{18})^{6-}$ ligands exert a lateral crystal field on the central Ln ion which is well suited to stabilize electrostatically a state with a prolate charge density [9,40,57]. The symmetrical and axially compressed coordination sphere favored large and axial magnetic moments. The high symmetry was even more necessary for the non-Kramer Tm(III) ion, where the ground state was found to be an almost degenerate doublet. The ground doublets were well separated in energy from the excited states (330 and 65 cm^{-1} for complexes **1** and **2**, respectively). This situation is likely to result in single-molecule magnet behavior [10,58], which was indeed found in **1** and **2**. Finally, we stress that compound **1** is a rare example of a thulium-based SMM.

Supplementary Materials: The following are available online at <http://www.mdpi.com/2312-7481/6/4/53/s1>, additional views of the crystal structures and crystal packing; additional magnetic data for **1** and **2**. Crystallographic data for the structural analysis have been deposited at the ICSD Database under depository numbers CSD-1960251 and CSD-1960252 for compounds **1** and **2**, respectively. This information may be obtained at http://www.fiz-karlsruhe.de/obtaining_crystal_structure_data.html. Figure S1: Molecular structure views for $\text{Na}_9[\text{Tm}(\text{W}_5\text{O}_{18})_2]\cdot 35\text{H}_2\text{O}$, **1**; Figure S2: Molecular structure views for $\text{Na}_9[\text{Yb}(\text{W}_5\text{O}_{18})_2]\cdot 35\text{H}_2\text{O}$, **2**; Figure S3: Powder X-Ray diffractograms of **1** and **2**; Figure S4: Compound **1**: (a) Frequency dependence of the out-of-phase ac signal (χ_M'') at 5 K with applied fields ranging from 0 and 1 T; (b) Field dependence of the relaxation time (τ) at 5 K; Figure S5: Frequency and temperature dependence of the in-phase (χ_M') and out-of-phase (χ_M'') ac signals for **1**; Figure S6: Cole-Cole plots for **1**; Figure S7: Temperature dependence of τ^{-1} of **1** with the best fit considering different processes; Figure S8: Compound **2**: Temperature dependence of the out-of-phase ac signal (χ_M'') at 2 K for different DC fields; Figure S9: Compound **2**: Temperature and frequency dependence of the in-phase (χ') and out-of-phase (χ'') ac susceptibilities recorded at 1.2 kOe dc field with a 3 Oe ac field; Figure S10: Cole-Cole ($\chi_M'' = f(\chi_M')$) plots for **2** between 2 and 6.25 K with the best fits to the generalized Debye model; Figure S11: Temperature dependence of τ^{-1} of **2** with the best fit supposing direct and Raman processes; Figure S12: SEM images of the morphology of triturated samples of **1** and **2**; Figure S13: SEM images of the powder of **1** in the characteristic X-ray emission; Figure S14: SEM images of the powder of **2** in the characteristic X-ray emission; Figure S15: SEM image of the surface of triturated samples of **1** and **2**; Table S1: Continuous Shape Measures calculations performed on **1** and **2**; Table S2: SF-CASSCF and SO-CASSCF energies for the $[\text{Ln}(\text{W}_5\text{O}_{18})_2]^{9-}$ complexes; Table S3: g factors of for the $[\text{Ln}(\text{W}_5\text{O}_{18})_2]^{9-}$ complexes deduced from SO-CASSCF calculations; Table S4: Crystal field and strength parameters (in cm^{-1}) for the $[\text{Ln}(\text{W}_5\text{O}_{18})_2]^{9-}$ complexes deduced from SO-CASSCF calculations.

Author Contributions: Conceptualization, investigation, S.V.R.; investigation, O.Y.M.; discussion of ideas and the results, commenting on the manuscript, G.M.R.; crystal structure investigations, S.K. and Y.A.K.; magnetic studies, C.P. and J.-P.S.; Ab-initio calculations, H.B.; writing—original draft preparation, C.P., O.M., S.V.R., and H.B.; writing—review and editing, J.P.S. All authors have read and agreed to the published version of the manuscript.

Funding: This work was carried out within the Fundamental Research Programme funded by the Ministry of Education and Science of Ukraine (grant ID 0119U100025), with support from Estonian Ministry of Education and Research through Grants IUT19-32, IUT19-3 and PUT692.

Acknowledgments: S.V.R. is grateful to Erasmus+ Université Toulouse III Paul Sabatier for a visiting grant.

Conflicts of Interest: The authors declare no conflict of interest.

References

1. Milios, C.; Winpenny, R.P. Cluster-Based Single-Molecule Magnets. In *Molecular Nanomagnets and Related Phenomena*; Gao, S., Ed.; Springer: Berlin/Heidelberg, Germany, 2015; Volume 164, pp. 1–109.
2. Ishikawa, N.; Sugita, M.; Ishikawa, T.; Koshihara, S.-y.; Youkoh, K. Lanthanide Double-Decker Complexes Functioning as Magnets at the Single-Molecular Level. *J. Am. Chem. Soc.* **2003**, *125*, 8694–8695. [[CrossRef](#)]
3. Rinehart, J.D.; Meihaus, K.R.; Long, J.R. Observation of a Secondary Slow Relaxation Process for the Field-Induced Single-Molecule Magnet $\text{U}(\text{H}_2\text{BPz}_2)_3$. *J. Am. Chem. Soc.* **2010**, *132*, 7572–7573. [[CrossRef](#)]
4. Woodruff, D.N.; Winpenny, R.E.P.; Layfield, R.A. Lanthanide Single-Molecule Magnets. *Chem. Rev.* **2013**, *113*, 5110–5148. [[CrossRef](#)] [[PubMed](#)]
5. Layfield, R.A. Organometallic Single-Molecule Magnets. *Organometallics* **2014**, *33*, 1084–1099. [[CrossRef](#)]
6. Guo, F.-S.; Bar, A.K.; Layfield, R.A. Main Group Chemistry at the Interface with Molecular Magnetism. *Chem. Rev.* **2019**, *119*, 8479–8505. [[CrossRef](#)] [[PubMed](#)]

7. Guo, F.-S.; Day, B.M.; Chen, Y.-C.; Tong, M.-L.; Mansikkamäki, A.; Layfield, R.A. Magnetic hysteresis up to 80 kelvin in a dysprosium metallocene single-molecule magnet. *Science* **2018**, *362*, 1400–1403. [[CrossRef](#)] [[PubMed](#)]
8. Vonci, M.; Giansiracusa, M.J.; Van den Heuvel, W.; Gable, R.W.; Moubaraki, B.; Murray, K.S.; Yu, D.; Mole, R.A.; Soncini, A.; Boskovic, C. Magnetic Excitations in Polyoxotungstate-Supported Lanthanoid Single-Molecule Magnets: An Inelastic Neutron Scattering and ab Initio Study. *Inorg. Chem.* **2017**, *56*, 378–394. [[CrossRef](#)]
9. AlDamen, M.A.; Cardona-Serra, S.; Clemente-Juan, J.M.; Coronado, E.; Gaita-Ariño, A.; Martí-Gastaldo, C.; Luis, F.; Montero, O. Mononuclear Lanthanide Single Molecule Magnets Based on the Polyoxometalates $[\text{Ln}(\text{W}_5\text{O}_{18})_2]^{9-}$ and $[\text{Ln}(\beta\text{-SiW}_{11}\text{O}_{39})_2]^{13-}$ (Ln(III) = Tb, Dy, Ho, Er, Tm, and Yb). *Inorg. Chem.* **2009**, *48*, 3467–3479. [[CrossRef](#)]
10. AlDamen, M.A.; Clemente-Juan, J.M.; Coronado, E.; Martí-Gastaldo, C.; Gaita-Ariño, A. Mononuclear Lanthanide Single-Molecule Magnets Based on Polyoxometalates. *J. Am. Chem. Soc.* **2008**, *130*, 8874–8875. [[CrossRef](#)]
11. Jia, J.-H.; Li, Q.-W.; Chen, Y.-C.; Liu, J.-L.; Tong, M.-L. Luminescent single-molecule magnets based on lanthanides: Design strategies, recent advances and magneto-luminescent studies. *Coord. Chem. Rev.* **2019**, *378*, 365–381. [[CrossRef](#)]
12. Meng, Y.-S.; Qiao, Y.-S.; Zhang, Y.-Q.; Jiang, S.-D.; Meng, Z.-S.; Wang, B.-W.; Wang, Z.-M.; Gao, S. Can Non-Kramers Tm(III) Mononuclear Molecules be Single-Molecule Magnets (SMMs)? *Chem. Eur. J.* **2016**, *22*, 4704–4708. [[CrossRef](#)]
13. Amjad, A.; Figuerola, A.; Sorace, L. Tm(III) complexes undergoing slow relaxation of magnetization: Exchange coupling and aging effects. *Dalton Trans.* **2017**, *46*, 3848–3856. [[CrossRef](#)]
14. Harriman, K.L.M.; Korobkov, I.; Murugesu, M. From a Piano Stool to a Sandwich: A Stepwise Route for Improving the Slow Magnetic Relaxation Properties of Thulium. *Organometallics* **2017**, *36*, 4515–4518. [[CrossRef](#)]
15. Peacock, R.D.; Weakley, T.J.R. Heteropoly tungstate complexes of the lanthanide elements. Part I. Preparation and reactions. *J. Chem. Soc. A* **1971**, 1836. [[CrossRef](#)]
16. Rozantsev, G.M.; Ignatyeva, V.V. Mathematical modeling of equilibria and the state of holmium heteropoly tungstate ions. *Russ. J. Inorg. Chem.* **2006**, *51*, 1509–1515. [[CrossRef](#)]
17. Rozantsev, G.M.; Ignatyeva, V.V. Ionic equilibria for hetero-10-tungstoneodimates: Study and modeling. *Russ. J. Coord. Chem.* **2007**, *33*, 641–647. [[CrossRef](#)]
18. Rozantsev, G.M.; Ignatyeva, V.V. Study of ionic equilibria and computation of thermodynamic characteristics of heteropoly anion formation in $\text{GdW}_{10}\text{O}_{36}^{9-}$ solution. *Russ. J. Inorg. Chem.* **2014**, *59*, 1045–1054. [[CrossRef](#)]
19. Sawada, K.; Yamase, T. Nonasodium decatungstodysprosate pentatriacontahydrate. *Acta Cryst. C* **2002**, *58*, i149–i151. [[CrossRef](#)]
20. Vonci, M.; Giansiracusa, M.J.; Gable, R.W.; Van den Heuvel, W.; Latham, K.; Moubaraki, B.; Murray, K.S.; Yu, D.; Mole, R.A.; Soncini, A.; et al. Ab initio calculations as a quantitative tool in the inelastic neutron scattering study of a single-molecule magnet analogue. *Chem. Commun.* **2016**, *52*, 2091–2094. [[CrossRef](#)]
21. Moriyasu, S.; Toshihiro, Y. Crystal Structure and Luminescence Site of $\text{Na}_9[\text{EuW}_{10}\text{O}_{36}] \cdot 32\text{H}_2\text{O}$. *Bull. Chem. Soc. Jpn.* **1993**, *66*, 444–449. [[CrossRef](#)]
22. Ozeki, T.; Yamase, T. Effect of lanthanide contraction on the structures of the decatungstolanthanoate anions in $\text{K}_3\text{Na}_4\text{H}_2[\text{LnW}_{10}\text{O}_{36}] \cdot n\text{H}_2\text{O}$ (Ln = Pr, Nd, Sm, Gd, Tb, Dy) crystals. *Acta Cryst. B* **1994**, *50*, 128–134. [[CrossRef](#)]
23. Yamase, T.; Ozeki, T.; Tosaka, M. Octasodium hydrogen decatungstogadolinate triacontahydrate. *Acta Cryst. C* **1994**, *50*, 1849–1852. [[CrossRef](#)]
24. Yamase, T.; Ozeki, T. Structure of $\text{K}_3\text{Na}_4\text{H}_2[\text{GdW}_{10}\text{O}_{36}] \cdot 21\text{H}_2\text{O}$. *Acta Cryst. C* **1993**, *49*, 1577–1580. [[CrossRef](#)]
25. Shiozaki, R.; Inagaki, A.; Ozaki, A.; Kominami, H.; Yamaguchi, S.; Ichihara, J.; Kera, Y. Catalytic behavior of a series of lanthanide decatungstates $[\text{Ln}(\text{III})\text{W}_{10}\text{O}_{36}^{9-}]$; Ln: La–Yb for H_2O_2 -oxidations of alcohols and olefins. Some chemical effects of the $4f^n$ -electron in the lanthanide(III) ion on the catalyses. *J. Alloys Comp.* **1997**, *261*, 132–139. [[CrossRef](#)]
26. Ozeki, T.; Yamase, T. Hexasodium trihydrogen decatungstosamarate octacosahydrate. *Acta Cryst. C* **1994**, *50*, 327–330. [[CrossRef](#)]
27. Casanova, D.; Alemany, P.; Bofill, J.M.; Alvarez, S. Shape and Symmetry of Heptacoordinate Transition-Metal Complexes: Structural Trends. *Chem. Eur. J.* **2003**, *9*, 1281. [[CrossRef](#)]

28. Alvarez, S.; Alemany, P.; Casanova, D.; Cirera, J.; Lluell, M.; Avnir, D. Shape maps and polyhedral interconversion paths in transition metal chemistry. *Coord. Chem. Rev.* **2005**, *249*, 1693–1708. [CrossRef]
29. Lluell, M.C.; Cirera, J.; Alemany, P.; Alvarez, S. *SHAPE, V2*; Universitat de Barcelona: Barcelona, Spain, 2010.
30. Huang, W.; Xu, J.; Wu, D.; Huang, X.; Jiang, J. Rhodamine-based field-induced single molecule magnets in Yb(III) and Dy(III) series. *New J. Chem.* **2015**, *39*, 8650–8657. [CrossRef]
31. Gavrikov, A.V.; Koroteev, P.S.; Efimov, N.N.; Dobrokhotova, Z.V.; Ilyukhin, A.B.; Kostopoulos, A.K.; Ariciu, A.-M.; Novotortsev, V.M. Novel mononuclear and 1D-polymeric derivatives of lanthanides and (η^6 -benzoic acid)tricarbonylchromium: Synthesis, structure and magnetism. *Dalton Trans.* **2017**, *46*, 3369–3380. [CrossRef] [PubMed]
32. Kahn, O. *Molecular Magnetism*; VCH: Weinheim, Germany, 1993.
33. Benelli, C.; Gatteschi, D. *Introduction to Molecular Magnetism: From Transition Metals to Lanthanides*; Wiley: Hoboken, NJ, USA, 2015.
34. Dekker, C.; Arts, A.F.M.; de Wijn, H.W.; van Duynveldt, A.J.; Mydosh, J.A. Activated dynamics in a two-dimensional Ising spin glass. *Phys. Rev. B* **1989**, *40*, 11243–11251. [CrossRef]
35. Cole, K.S.; Cole, R.H. Dispersion and Absorption in Dielectrics I. Alternating Current Characteristics. *J. Chem. Phys.* **1941**, *9*, 341–351. [CrossRef]
36. Pescia, J. La Relaxation des spins électroniques avec le réseau (Théorie élémentaire et méthodes de mesure du temps T₁). *J. Phys. France* **1966**, *27*, 782–800. [CrossRef]
37. Rechkemmer, Y.; Breitgoff, F.D.; van der Meer, M.; Atanasov, M.; Hakl, M.; Orlita, M.; Neugebauer, P.; Neese, F.; Sarkar, B.; van Slageren, J. A four-coordinate cobalt(II) single-ion magnet with coercivity and a very high energy barrier. *Nat. Commun.* **2016**, *7*, 10467. [CrossRef]
38. Cardona-Serra, S.; Clemente-Juan, J.M.; Coronado, E.; Gaita-Ariño, A.; Camón, A.; Evangelisti, M.; Luis, F.; Martínez-Pérez, M.J.; Sesé, J. Lanthanoid Single-Ion Magnets Based on Polyoxometalates with a 5-fold Symmetry: The Series [LnP₅W₃₀O₁₁₀]₁₂– (Ln³⁺ = Tb, Dy, Ho, Er, Tm, and Yb). *J. Am. Chem. Soc.* **2012**, *134*, 14982–14990. [CrossRef]
39. Jung, J.; Islam, M.A.; Pecoraro, V.L.; Mallah, T.; Berthon, C.; Bolvin, H. Derivation of Lanthanide Series Crystal Field Parameters From First Principles. *Chem. Eur. J.* **2019**, *25*, 15112–15122. [CrossRef]
40. Rinehart, J.D.; Long, J.R. Exploiting single-ion anisotropy in the design of f-element single-molecule magnets. *Chem. Sci.* **2011**, *2*, 2078. [CrossRef]
41. Korostelev, P.P. Preparation of Solutions for Chemical Analysis. *Nauka Mosc.* **1964**, 401.
42. Shvartsenbakh, G.; Flashka, G. Complexometric Titration [Russian translation]. *Khimiya Mosc.* **1970**, 360.
43. *CrysAlisPro*; Agilent Technologies Ltd.: Oxfordshire, UK, 2014. Available online: <https://journals.iucr.org/e/services/stdswrefs.html> (accessed on 1 October 2020).
44. Clark, R.C.; Reid, J.S. The analytical calculation of absorption in multifaceted crystals. *Acta Cryst. A* **1995**, *51*, 887–897. [CrossRef]
45. Dolomanov, O.V.; Bourhis, L.J.; Gildea, R.J.; Howard, J.A.K.; Puschmann, H. OLEX2: A complete structure solution, refinement and analysis program. *J. Appl. Cryst.* **2009**, *42*, 339–341. [CrossRef]
46. Sheldrick, G. Crystal structure refinement with SHELXL. *Acta Cryst. C* **2015**, *71*, 3–8. [CrossRef]
47. Sheldrick, G. SHELXT—Integrated space-group and crystal-structure determination. *Acta Cryst. A* **2015**, *71*, 3–8. [CrossRef]
48. Roos, B.O.; Lindh, R.; Malmqvist, P.A.; Veryazov, V.; Widmark, P.O. Main group atoms and dimers studied with a new relativistic ANO basis set. *J. Phys. Chem. A* **2004**, *108*, 2851–2858. [CrossRef]
49. Roos, B.O.; Lindh, R.; Malmqvist, P.-Å.; Veryazov, V.; Widmark, P.-O. New relativistic ANO basis sets for actinide atoms. *Chem. Phys. Lett.* **2005**, *409*, 295–299. [CrossRef]
50. Casarrubios, M.; Seijo, L. The ab initio model potential method: Third-series transition metal elements. *J. Chem. Phys.* **1999**, *110*, 784–796. [CrossRef]
51. Roos, B.O.; Taylor, P.R.; Sigbahn, P.E.M. A complete active space SCF method (CASSCF) using a density matrix formulated super-CI approach. *Chem. Phys.* **1980**, *48*, 157–173. [CrossRef]
52. Malmqvist, P.-Å.; Roos, B.O.; Schimmelpfennig, B. The restricted active space (RAS) state interaction approach with spin-orbit coupling. *Chem. Phys. Lett.* **2002**, *357*, 230–240. [CrossRef]
53. Hess, B.A. Relativistic electronic-structure calculations employing a two-component no-pair formalism with external-field projection operators. *Phys. Rev. A* **1986**, *33*, 3742–3748. [CrossRef] [PubMed]

54. Heß, B.A.; Marian, C.M.; Wahlgren, U.; Gropen, O. A mean-field spin-orbit method applicable to correlated wavefunctions. *Chem. Phys. Lett.* **1996**, *251*, 365–371. [[CrossRef](#)]
55. Bolvin, H. An Alternative Approach to the g-Matrix: Theory and Applications. *Chem. Phys. Chem.* **2006**, *7*, 1575–1589. [[CrossRef](#)]
56. Ungur, L.; Chibotaru, L.F. Ab Initio Crystal Field for Lanthanides. *Chem. Eur. J.* **2017**, *23*, 3708–3718. [[CrossRef](#)] [[PubMed](#)]
57. Martínez-Pérez, M.J.; Cardona-Serra, S.; Schlegel, C.; Moro, F.; Alonso, P.J.; Prima-García, H.; Clemente-Juan, J.M.; Evangelisti, M.; Gaita-Ariño, A.; Sesé, J.; et al. Gd-Based Single-Ion Magnets with Tunable Magnetic Anisotropy: Molecular Design of Spin Qubits. *Phys. Rev. Lett.* **2012**, *108*, 247213. [[CrossRef](#)] [[PubMed](#)]
58. Baldoví, J.J.; Clemente-Juan, J.M.; Coronado, E.; Duan, Y.; Gaita-Ariño, A.; Giménez-Saiz, C. Construction of a General Library for the Rational Design of Nanomagnets and Spin Qubits Based on Mononuclear f-Block Complexes. The Polyoxometalate Case. *Inorg. Chem.* **2014**, *53*, 9976–9980. [[CrossRef](#)] [[PubMed](#)]

Publisher’s Note: MDPI stays neutral with regard to jurisdictional claims in published maps and institutional affiliations.



© 2020 by the authors. Licensee MDPI, Basel, Switzerland. This article is an open access article distributed under the terms and conditions of the Creative Commons Attribution (CC BY) license (<http://creativecommons.org/licenses/by/4.0/>).